Current Research in Food Science 9 (2024) 100864

Contents lists available at ScienceDirect

Current Research in Food Science

journal homepage: www.sciencedirect.com/journal/current-research-in-food-science

Energy insufficiency induced by high purine diet: Catalysts for renal impairment in hyperuricemia nephropathy rat model

Zhenxiong Zhao [a], Zhikun Li [b], Yubin Xu [a], Shiqi Zhao [c], Qing Fan [c,*], Zhencang Zheng [a,**]

[a] Taizhou Central Hospital (Taizhou University Hospital), Taizhou, Zhejiang 318000, China
[b] Shandong Institute for Food and Drug Control, Jinan, 250117, China
[c] Shandong Cancer Hospital and Institute, Shandong First Medical University and Shandong Academy of Medical Sciences, Jinan 250117, China

ARTICLE INFO

Handling Editor: Dr. Yeonhwa Park

Keywords:
Hyperuricemia nephropathy
High purine diet
Metabolomic
Proteomic
Fatty acid β-oxidation

ABSTRACT

A high purine diet emerges as a significant risk factor for hyperuricemia, and this diet may potentiate hyperuricemia nephropathy. Despite this, the mechanistic underpinnings of kidney damage precipitated by a high purine diet warrant further research. In the current investigation, a hyperuricemia nephropathy rat model was developed through induction via a high purine diet. Subsequently, metabolomic and proteomic analyses were employed to explore the metabolic characteristics of the kidney and shed light on the corresponding mechanistic pathway. Finally, fluorescence imaging and ^{18}F-fluorodeoxyglucose positron emission tomography computed tomography (^{18}F-FDG-PET/CT) were utilized to validate the overarching energy metabolism state. The results revealed extensive damage to the kidneys of hyperuricemia nephropathy rats following eight weeks of induction via a high purine diet. We used metabolomic to found that acyl carnitines and L-carnitine reduced in high purine diet group, indicated abnormal fatty acid metabolism. Irregularities were discerned in metabolites and enzymes associated with fatty acid β-oxidation, glycolysis, and oxidative phosphorylation within the kidneys of hyperuricemia nephropathy rats by proteomic and co-expression network analysis. The application of fluorescence imaging and ^{18}F-FDG-PET/CT substantiated the inhibition of fatty acid β-oxidation and glycolysis within the kidneys of hyperuricemia nephropathy rats. On the contrary, a compensatory enhancement in the function of oxidative phosphorylation was observed. Given that the primary energy supply for renal function was derived from the metabolic pathway of fatty acids β-oxidation, any disruption within this pathway could contribute to a deficit in the energy provision to the kidneys. Such an energy insufficiency potentially laid the groundwork for eventual renal impairment. In addition, inhibition of the peroxisome proliferator-activated receptors signaling pathway was noted in the present findings, which could further exacerbate the impediment in the β-oxidation function. In conclusion, it was discerned that a deficiency in energy supply plays a critical role in the kidney injury in hyperuricemia nephropathy rats, thereby endorsing paying more attention to renal energy supply in the therapy of hyperuricemia nephropathy.

1. Introduction

In the human organism, purines undergo a transformation process, culminating in the formation of uric acid (McCormick and Choi, 2024; Tran et al., 2024). These purines are prevalent in numerous food types, with a particular abundance in meat and seafood. A diet with high purine content, referred to as a high purine diet (HPD), can disrupt the natural purine metabolic processes within the body, potentially leading to a condition known as hyperuricemia (Y. F. Gao et al., 2023; Hao et al., 2024; Mehmood et al., 2024).

Hyperuricemia, a disease characterized by the excessive presence of uric acid in the bloodstream, has long been associated with genetic factors (J. Chen et al., 2023). It is frequently found in conjunction with obesity, diabetes, and chronic renal failure - all of which are multifactorial genetic diseases linked to Hyperuricemia (Joosten et al., 2020). Contemporary nutritional science suggests that the primary cause of hyperuricemia is a diet rich in purines, fructose, and protein (Lubawy and Formanowicz, 2023). Such a diet can disrupt purine metabolic processes, leading to an imbalance in uric acid levels, the final product of purine metabolism. This imbalance can result in an accumulation of

* Corresponding author.
** Corresponding author.
E-mail addresses: fanqing@sdfmu.edu.cn (Q. Fan), zhengzc6004@tzzxyy.com (Z. Zheng).

https://doi.org/10.1016/j.crfs.2024.100864
Received 8 August 2024; Received in revised form 17 September 2024; Accepted 20 September 2024
Available online 21 September 2024

uric acid in the bloodstream, triggering a range of adverse repercussions, including potential organ damage. The kidney, the primary organ responsible for uric acid excretion, filters and eliminates over 70% of the body's uric acid through urine (Dalbeth et al., 2021). As such, an excessive amount of uric acid can cause significant damage to the kidneys.

Hyperuricemic nephropathy (HN), a form of chronic kidney disease (CKD), has been reported to be correlated with hyperuricemia (Hou et al., 2023). An abundance of evidence suggests that elevated uric acid levels can initiate a cascade of renal complications, including renal inflammation (Wang et al., 2024), tubulointerstitial fibrosis (Liu et al., 2021), uric acid nephrolithiasis (Cao et al., 2024), and chronic interstitial glomerulonephritis. These conditions can eventually lead to HN, CKD, or even end-stage renal disease (ESRD). Approximately 20% of untreated hyperuricemia patients are at risk of developing HN(Bardin et al., 2021). A diet characterized by excessive purine consumption can exacerbate the risk of hyperuricemia and HN, thus becoming a significant risk factor.

The prevailing belief is that an overabundance of uric acid accumulated in the renal tissue, typically following excessive purine intake, instigates inflammatory chronic kidney disease (Zhao et al., 2022). Nonetheless, a more nuanced understanding of the pathogenesis of Hyperuricemic Nephropathy (HN) triggered by high purine diet (HPD) necessitates further in-depth exploration. Contemporary studies have furnished evidence that HPD might amplify the production of pro-inflammatory cytokines (IL-1β and IL-18) by stimulating NLRP3 (He et al., 2023). Moreover, the uric acid inflammatory impact on tubular cells could be mediated through the High Mobility Group Box Chromosomal Protein 1 (HMGB1), which enhances the Nuclear Factor Kappa-B (NF-κB) signaling (Kim et al., 2015).

In a rat model mimicking HN, the consumption of surplus adenine escalated Src phosphorylation, severe glomerular sclerosis, and renal interstitial fibrosis (Xiong et al., 2024). Furthermore, oxidative stress instigated by HPD has been identified as a pivotal contributor to hyperuricemic nephropathy (Li et al., 2024). The impairment of the NRF2-activated antioxidant pathway, driven by HPD, has been recognized as a catalyst for oxidative damage during HN progression (Qiao et al., 2023). In a similar vein, HPD also disrupts the equilibrium of intestinal micro-ecology. Beyond its inherent genetic factors, the gut microbiota plays a fundamental role in the pathogenesis of HN. Disruptions in urease expression and ammonia metabolism within the gut microbiota due to HPD could trigger renal damage (Pan et al., 2020). While advancements have been made in researching the impact of HPD on HN, there is a scarcity of studies focusing on the renal glucose and lipid metabolism induced by HPD.

The metabolic processes of glucose and lipids bear significant implications on the inception and progression of renal diseases. Renal cell carcinoma is conspicuously characterized by an imbalance in aerobic glycolysis, fatty acid metabolism, and the utilization of tryptophan glutamine, all of which are intricately intertwined with mitochondrial function (Qi et al., 2021). It is noteworthy that mitochondria, the intracellular organelles mandated with the orchestration of biological glucose and lipid metabolic processes in mammalian cells, assume a central role within this complex interplay. A manifestation of mitochondrial dysfunction can instigate a series of events, including inflammatory responses, disrupted mitochondrial autophagy, and related processes, eventually leading to the onset of renal damage (X. Zhao et al., 2024a). Heightened lipid peroxidation has been observed in mice models with acute aristolochic acid nephropathy. This perturbation in lipid metabolism can escalate the production of reactive oxygen species (ROS), thereby inducing renal damage (Yang et al., 2024). Hence, delving into the impact of hyperuricemia-inducing purine diet on renal glucose and lipid metabolism bears significant relevance.

2. Material and methods

2.1. Animals and experimental protocol

Male Sprague Dawley (SD) rats (120 g ± 10 g, 4–6-week-old) were purchased from Zhejiang Vital River Company (Hangzhou, China) and they were kept under 12 h light/dark cycles, and allowed free access to food and water. All the rats have adapted to the environment for 1 week before the experiment started. The experiment was carried out in strict accordance with the ethical guidelines for experimental animals, and was approved by the Animal Ethics Committee of the Experimental Animal Institute of Taizhou University (No. TZXY-2022-20221052). Twenty-eight SD rats were randomly assigned into two groups, comprising fourteen animals each. One group served as the control, while the other was designated as the model group. The control group was fed with regular feed (corn flour 50%, soybean meal 23%, fish meal 10% wheatmeal 10% soybean oil 5%, salt 1%, multi-vitamins 0.5%, composite mineral elements 0.5%). The model group was fed with a special folder (by adding 10% yeast and 0.15% adenine in above regular feed) for 8 weeks. The animals were fasted overnight (for about 12 h) on the last day of experimental model before the induction of anesthesia or the collection of blood samples.

2.2. H&E and masson staining

The implemented method was initiated with the dewaxing of pre-prepared paraffin sections via a xylene I and II treatment at a duration of 5 min each. This procedure subsequently proceeded to gradient treatment with ethanol, specifically involving 5 min in anhydrous ethanol, 2 min in 95% ethanol, two additional minutes in 80% ethanol, and concluded with a 2-min treatment in 70% ethanol. Subsequently, the dewaxed tissue sections underwent a 2-min distilled water rinse, leading to a 20-min staining process with hematoxylin dye. This was promptly followed by rinsing with tap water. Upon conclusion of the differentiation process which lasted for 30 s, the tissue samples were submerged in water for 15 min, before staining with eosin solution was carried out for 30 s with another tap water rinse. While immersed in water for 5 min, a dehydration process was undertaken via an ethanol gradient, with progression to clarification via xylene, and ultimately, neutral resin embedding. Observation of specimens was administered under optical microscope examination.

Regarding the Masson staining procedure, paraffin sections were dewaxed using xylene and dyed with Weigert iron hematoxylin staining solution for 5 min. A differentiation stage followed using acidic ethanol for 5 s and was complemented by a water rinse. Application of a Masson blue solution for 3 min allowed for repigmentation before sections were rinsed with distilled water for 1 min. The application of Lichunhong Magenta staining solution followed for 5 min, subsequently leading to a rinse with a weak acid working solution, a mixture of distilled water and weak acid in a 2:1 ratio, for 1 min. This was followed by a 2-min phosphomolybdic acid treatment, another rinse with weak acid, and staining with aniline blue solution for 2 min. After a final rinse with the weak acid working solution, rapid dehydration occurred with 95% ethanol, followed by absolute ethanol three times. Transparency induced by xylene three times preceded the embedding with neutral resin. Lastly, sections were examined and documented under an optical microscope.

2.3. Creatinine, urea nitrogen, and uric acid measurement in serum

Evaluation of renal function was accomplished through the determination of serum levels of creatinine, urea nitrogen (BUN), and uric acid. In order to facilitate these assessments, blood samples (200 μl) were extracted from the rats and subjected to centrifugation at a speed of 2000 revolutions per minute for a duration of 5 min. Subsequently, serum samples were isolated and subjected to analysis via a detection

kit. The detailed steps see the supplementary material.

2.4. Metabolomic analysis

Assessments in metabolomics were conducted utilizing both Liquid Chromatography Tandem Mass Spectrometry (LC-MS/MS, Thermo QE plus) and Gas Chromatography Tandem Mass Spectrometry (GC-MS, Agilent 8890-5977B). Specified chromatographic columns employed included ACQUITY UPLC HSS T3 (Waters, 100 mm × 2.1 mm, 1.8 μm) and DB-5MS (Agilent, 30 m × 0.25 mm × 0.25 μm).

Sample preparation involved grinding in an 80% methanol solution, with an L-2-chlorophenylalanine concentration of 4 μg/mL. For LC-MS/MS analysis, the disrupted homogenate was further processed through a 10-min sonication in an ice bath. Post centrifugation, the supernatant was isolated for LC-MS/MS examination. Mobile phases deployed included water (A) and acetonitrile (B), both containing 0.1% formic acid with flow rate of 0.35 mL/min. The elution gradient program was as follows, 0 min, A:B = 95:5 (%); 2 min, A:B = 95:5 (%); 4 min, A:B = 70:30 (%); 8 min, A:B = 50:50 (%); 10 min, A:B = 20:80 (%); 14 min, A:B = 0:100 (%); 15 min, A:B = 0:100 (%). Both of ESI positive and negative modes were used in mass spectrometry. A detailed presentation of mass spectrometry parameters is available in Table 1.

For GC-MS procedures, the homogenate was extracted with 150 μL chloroform followed by centrifugation, with the resulting lower supernatant then selected for GC-MS examination. Carrier gas (Helium) flow rate was fixed at 1.0 mL/min with an injector temperature of 260 °C. The initial column temperature was set at 60 °C, maintained for 0.5 min before procedurally increasing to 210 °C at 8 °C/min, then progressing to 305 °C at 20 °C/min. Ionization was performed using an Electron Impact (EI) ion source, with a collision voltage of 70 eV. Ion source temperature and quadrupole temperature were set at 230 °C and 150 °C, respectively. Data analysis refer to the methods previously reported (Q. Chen et al., 2022).

2.5. Proteomics measurements

Proteomics was performed with a Q Exactive HF Mass Spectrometer (ThermoFisher) using a data-independent acquisition tandem mass tags (TMT) protocol. Briefly, proteins in the kidney were extracted and measured by the bicinchoninic acid (BCA) method. After trypsin enzymolysis, the peptides were marked by the TMT reagent. An Agilent 1100 HPLC system was used to separate peptides with an Agilent Zorbax Extend C18 column (2.1 × 150 mm, 5 μm). Proteomic analysis was performed using nanoflow liquid chromatography (EASY-nLC 1200, ThermoFisher) coupled with mass spectrometry (Q Exactive HF mass spectrometer; ThermoFisher). The profile mode of an Orbitrap at a resolution of 60,000 was used to acquire a full-mass scan (350–1500 m/z). Peptide segments with the highest top 20 were chosen for further LC−MS/MS analysis. All spectra were acquired using data dependent high-energy collision splitting in positive ion mode with a collision energy of 32 eV. The secondary fragment was performed with a resolution of 45,000.

Table 1
Mass spectrometry parameters of metabolomics analysis.

Parameters	ESI+	ESI-
Spray Voltage (V)	3800	−3000
Capillary Temperature (°C)	320	320
Aux gas heater temperature (°C)	350	350
Sheath Gas Flow Rate (Arb)	35	35
Aux gas flow rate (Arb)	8	8
S-lens RF level	50	50
Mass range (m/z)	100–1200	100–1200
Full ms resolution	70000	70000
MS/MS resolution	17500	17500

2.6. Protein identification and database searching

The spectra generated by LC–MS/MS were searched in a database of ProteomeDiscoverer (Version 2.4.1.15, ThermoFisher). The precursor mass was set to 20 ppm, and the fragment ion mass tolerance was set to 20 ppm. Methionine oxidation and protein N-terminal acetylation were set as variable modifications, and carbamidomethyl was set as a fixed modification. Two missed cleavages for trypsin were allowed. A false discovery rate of 1% was set at both the peptide and protein levels to filter the results. MaxQuant with label-free quantification was used for protein quantification. A minimum peptide ratio count of two was required, and only unmodified peptides were used for relative quantification. A total of 6638 proteins were identified from serum samples. The expression matrix was normalized by normalizeBetweenArrays function of the R package limma, which is an optimal normalization method commonly used in proteomics data analysis. Normalized protein abundance was log2-transformed and used in all quantitative analyses. The missing values were imputed with the minimum of the proteomic data.

2.7. Co-expression network analysis

Network analysis was performed to identify modules of co-expressed proteins. The WGCNA package in R was used to normalize protein abundance to define protein co-expression networks. The function WGCNA:blockwiseModules was used with the following settings: soft threshold power β = 2, deepSplit = 4, minModuleSize = 10, mergeCutHeight = 0.05, threshPercent = 50, and mergePercent = 25, and all other parameters were set to the default. Soft threshold power β defined strong correlations between proteins and penalized weak correlations. Module eigenprotein correlation value kME is defined as a module membership measure, which was calculated by Pearson correlations between each protein and each module eigenprotein. The percentage of module members checked for kME overlap of 50% (threshPercent = 50) and the threshold for merging modules with a high common kME. intramodule of 25% (mergePercent = 25) were used to reduce the number of modules. The topological overlap matrix measured the network connectivity of a protein, which is defined as the sum of its adjacency with all other proteins for network generation. Hierarchical clustering analysis was conducted based on 1-topological overlap matrix, with a merge cutoff height of 0.05, to classify proteins with similar expression patterns.

2.8. Fluorescence imaging

The fluorescence imagines of rats' kidneys were performed on an IVIS optical imaging system. Fatty acid metabolism was assessed using BODIPY FL C_{16} (Thermo Fisher Scientific Inc.) as a probe, and mitochondrial membrane potential was assessed by tetramethylrhodamine ethyl ester perchlorate (TMRE, MedChemExpress). The wavelength of the excited and the emitted spectrum of BODIPY FL C_{16} and TMRE were 505/512 and 550/576 nm, respectively. Both of the fluorescent probes were injected via the tail vein, the administered doses were 0.3 μM/kg for BODIPY FL C_{16} and 1 μM/kg for TMRE, respectively. The rats were killed and the kidneys were taken out after 30 min of tail vein injection. And then, fluorescence imaging experiments were carried out immediately.

2.9. In vivo fluorodeoxyglucose-positron emission tomography/computed tomography (FDG-PET/CT) imaging

Following an 8-week period, rats were subjected to Positron Emission Tomography/Computed Tomography (PET/CT) analysis. The PET/CT imaging was executed using the Inveon MM Platform (Siemens Preclinical Solutions, Knoxville, Tennessee, USA). The device, equipped with a computer-controlled bed, offered a transaxial field of view (FOV)

of 8.5 cm and an axial FOV of 5.7 cm. Anesthesia was administered to the animals via 2% isoflurane in O2 gas ahead of the [18F]-Fluorodeoxyglucose (FDG) injection, comprising of a solitary 0.1 ml FDG injection with an activity of 10 MBq, intravenously via the tail vein. Subsequent to the injection, animals were promptly revived and returned to the anesthesia cage.

Two hours post-tracer injection, the animals were anesthetized for a second time, laid in a prone position on the PET scanner bed, optimally positioned near the central field of view, and then maintained under consistent anesthesia with 1.5% isoflurane in oxygen administered at a flow rate of 2 L/min. The scanning procedure was performed using the Inveon Acquisition Workplace software (version 1.5.0.28). Ahead of the PET scan, a 10-min CT X-ray was conducted for attenuation correction, utilizing 80Kv power and 500 μA with an exposure time of 1100ms. Following this, static PET scans were performed for a duration of 10 min. Images were subsequently reconstructed using an OSEM3D (Three-Dimensional Ordered Subsets Expectation Maximum) algorithm, succeeded by MAP (Maximization/Maximum a Posteriori) or FastMAP, provided by the IAW. The 3D regions of interest (ROIs) were drawn over the heart guided by CT images and tracer uptake was measured using the software of Inveon Research Workplace (IRW) 3.0, and then mean standardized uptake values (SUVs) were calculated.

2.10. Statistical analysis

The statistical analyses were conducted using two-way ANOVA and Student's t-test with GraphPad Prism Version 8.01 (GraphPad Software, CA, United States). The data are expressed as the means ± standard deviation and p values < 0.05 were considered statistically significant. Omics analysis was performed using R software unless noted otherwise. Principal component analysis (PCA) was performed by using the "PCA" function in the FactoMineR package. Orthogonal partial least-squares discrimination analysis (OPLS-DA), pathway analysis and visualization were performed by using MetaboAnalyst 5.0 (http://www.metaboanalyst.ca/MetaboAnalyst/).

3. Results

3.1. Hyperuricemia nephropathy model establishment induced by HPD

Implementation of a hyperuricemia nephropathy model was achieved through an 8-week regimen of a high-purine diet comprising 10% yeast powder and 0.15% adenine. Evaluations, as evidenced by Fig. 1A, revealed a noticeable discolouration in the kidney wherein severe lesions developed following 8 weeks of the HPD treatment. H&E staining unveiled significant vacuolar degeneration of renal tubules in addition to a markedly broadened interstitium (marked with red arrow). Observations from Masson staining explicated an expansion of the renal interstitium and subsequent fibrosis in SD rats (marked with red arrow). Biochemical measurements including those for serum uric acid, creatinine, and urea nitrogen levels, indicated substantial elevations in the model group relative to those observed for rats maintained on a regular diet, as presented in Fig. 1C and D. The documented findings collectively validated the significant nephrotoxic impact inflicted by the high-purine diet on rat kidneys, as discerned from both morphological and pathological evaluations.

3.2. Untargeted metabolomics profiling of kidney from rats with HN

Employing the techniques of both Liquid Chromatography-Mass Spectrometry (LC-MS/MS) and Gas Chromatography-Mass Spectrometry (GC-MS), an untargeted metabolomic study was performed on hyperuricemia nephropathy (HN) rat specimens. The LC-MS/MS metabolomics approach yielded the identification of a total of 8003 metabolites, predominantly constituting lipids or lipid-like molecules (32.69%) and derivatives of organic acids (18.55%) (Refer to Fig. S1). Meanwhile, the GC-MS metabolomics method led to the identification of 764 metabolites. The highest proportions of superclass metabolites were constituted by organic acids and their derivatives (24.19%), organic oxidation compounds (23.39%), and lipids or lipid-like molecules (20.70%). The principal component analysis (PCA) plot of Quality Control (QC) samples showed tight clustering in both the LC-MS and GC-MS platforms, thus confirming the satisfactory repeatability of the analysis during these studies (Refer to

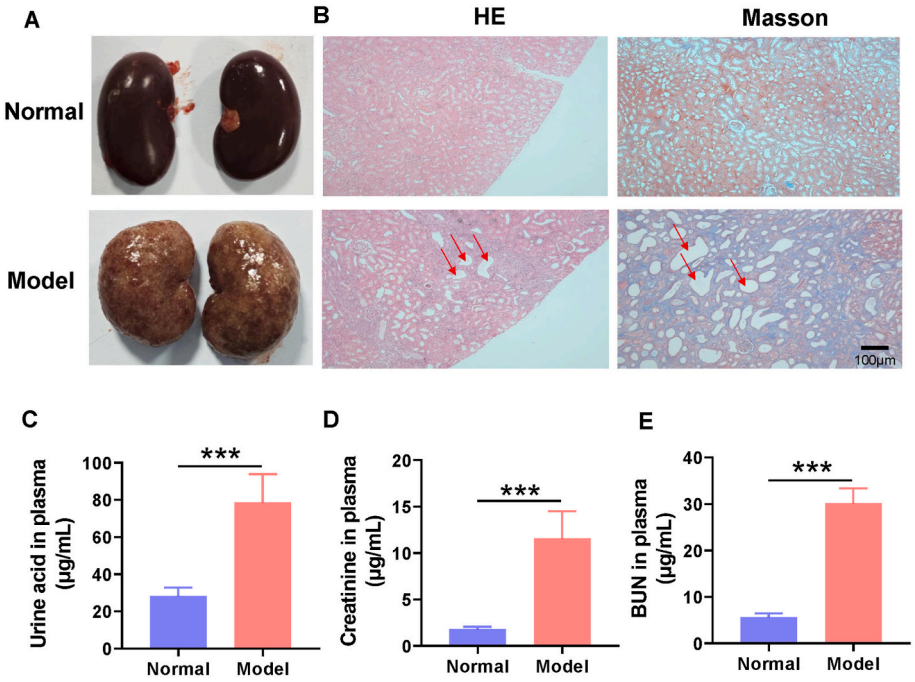

Fig. 1. Biological index for model establishment. (A)Kidney morphology of normal and model group. (B) H&E pathological staining and Masson staining. (C–D) The serum level of uric acid, creatinine and urea nitrogen (BUN) in normal group and model group. Data are expressed as mean ± SD (n = 6), ***p < 0.001 vs. CON group.

Fig. S2). Multivariate statistical analysis led to the generation of metabolites PCA, partial least squares discrimination analysis (PLS-DA) and Orthogonal PLS-DA (OPLS-DA) results which have been represented in Fig. 2A across both the LC-MS and GC-MS platforms. Results from PLS-DA and OPLS-DA indicated that the metabolites in the kidneys of HN rats bore significant influence due to the High-Purine Diet (HPD). Differentially expressing metabolic elements, exhibiting a cut-off value of a Benjamini–Hochberg adjusted filter of less than 0.05 and log2 (FC) greater than 0, were identified as 248 (146 upregulated and 102 downregulated) and 43 (27 upregulated and 16 downregulated) in LC-MS and GC-MS platforms respectively, with respect to HN rat samples (Refer to Fig. 2B and C). The heatmap of metabolites is represented in Fig. 2D and E. Notably, in the top 50 heatmap of the LC-MS platform (Fig. 2D), 6 metabolites showed upregulation, while 44 revealed downregulation in HN rats. The metabolic constituent L-carnitine, marked with a green dot in Fig. 2D, showed a significant decline in HN rats. Similar trends were observed for metabolites such as o-propanoyl-carnitine, linoelaidylcarnitine, 5-methylheptadecanoylcarnitine, 2-hydroxydocosanoylcarnitine, 3-hydroxybutyrylcarnitine and (13Z)-octadec-13-enoylcarnitine, all of which are marked with a green dot. Fig. 2E represents the top 40 heatmap of the GC-MS platform, indicating the upregulation of 15 and downregulation of 25 metabolites in HN rats. Post HPD induction, a significant reduction in Maleic acid (denoted by a green triangle) was observed, along with the accumulation of oleic acid and palmitic acid (indicated by a green dot) in the kidney of HN rats. The alterations in these metabolites allude to a disruption in both lipid and glucose metabolism in the kidney of HN rats.

Fig. 3Aand B displays the Z-scores of the top 20 metabolites. The results from LC-MS indicate a diminishment in the normal levels of the majority of the metabolites in the rat kidneys following the HPD, excluding L-glutamine. Echoing the results from the heatmap, a significant increase was noticed in the fatty acids in HN rats. The KEGG IDs of differential metabolites were employed to perform pathway enrichment analysis and consequently, the top 20 metabolic pathway enrichment results were obtained (Refer to Fig. 3C and D), which includes butanoate metabolism, biosynthesis of unsaturated fatty acids and pentose and glucuronate interconversions among others.

3.3. Proteomic analyses

To investigate the potential aberrations in glucose and lipid metabolizing enzymes in rat kidneys as a consequence of HPD, quantitative proteomic analysis was performed on kidneys from both normouricemic and Hyperuricemic Nephropathy (HN) rats. The protein profiling was executed utilizing the technique of Tandem Mass Tagging (TMT) Quantitative proteomic analysis, yielding detection of a total of 57470 peptides and identification of 6638 proteins. The Principal Component Analysis (PCA) of these 6638 independent proteins showed that distinct and non-overlapping clusters were formed by the different samples and their respective replicates (Refer to Fig. S3). Analysis of differential protein expression, as represented by the heatmap and volcano plot (Fig. 4A and B), revealed upregulation of 17 protein expressions, and downregulation of 21 proteins in HN rats. Amongst the downregulated proteins, NADH-Ubiquinone Oxidoreductase Chain 2 (ND2, A0A0A1G491) and Glyceraldehyde-3-Phosphate Dehydrogenase (GAPDH, A0A0G2K7M1), both critical in glucose metabolism, were denoted by a red dot in Fig. 4A. Expression of Cytochrome *c* Oxidase subunit 2 (COX2, P00406), a crucial enzyme in cellular electron transport, was upregulated in HN rats, indicated by a blue dot. Proteins including Long Chain Fatty Acid CoA Ligase 6 (ACSL6, A0A8I5ZPS9), 2,4-Dienoyl-CoA Reductase (DECR1, Q64591), Acetyl-CoA Acyltransferase-1 B (ACAA1B, P07871), and Carnitine O-Octanoyltransferase (CROT, Q6GMN6) were all downregulated following HPD administration, each bearing vital roles in fat metabolism, are indicated with a green triangle. Fig. 4C revealed the results from correlation analysis, reflecting the complex interrelationship among these proteins.

3.4. Functional enrichment analysis of differential proteins

To elucidate the alterations in biological functions provoked by the differential protein expression in the kidneys of Hyperuricemic Nephropathy (HN) rats, both Gene Ontology (GO) and Kyoto Encyclopedia of Genes and Genomes (KEGG) enrichment analyses were conducted. The list of species proteins formed the basis for comparison, with the differential protein list serving as the group selected from this foundational list. A hypergeometric distribution test granted the computation of p-values indicative of significant enrichment of functional sets within the differential protein list, which was further refined through correction via the Benjamini & Hochberg multiple test to achieve the False Discovery Rate (FDR). The results stemming from the GO enrichment analysis are represented in Fig. 5A–C and Fig. S4. Examination of the top 30 and 15 GO terms (Fig. 5A and B) indicated the perturbation of biological processes such as fatty acid β-oxidation and mitochondrial electron transport due to the High-Purine Diet (HPD); notable shifts were observed in cellular components like the integral component of membrane, peroxisome, mitochondrion, mitochondrial inner membrane, cytosol, and respirasome; molecular functions including protein homodimerization activity, cytochrome-c oxidase activity and NADH dehydrogenase activity also reflected imbalance. The specifics regarding upregulation or downregulation are presented in Fig. S4. The chord diagram of GO enrichment analysis results (Fig. 5C) revealed HPD-induced inhibitory influence on the expression of all proteins implicated in fatty acid β-oxidation and peroxisome; a variation was observed in the expression of proteins associated with respirasome, mitochondrion, mitochondrial inner membrane, and protein homodimerization. The results emanating from the KEGG enrichment analysis (Fig. 5D–F) signified an HPD-induced downgrade in fatty acid degradation, peroxisome proliferator-activated receptors (PPARs) signaling pathway, peroxisome and butanoate metabolism. Conversely, a notable enhancement in oxidative phosphorylation (indicated by a red dot) was manifested in the kidneys of HN rats as displayed in Fig. 5F.

3.5. Integrative analysis of metabolomics and proteomes

Utilizing the metabolomics and proteomics data, a Kyoto Encyclopedia of Genes and Genomes (KEGG) enrichment analysis was performed. The analysis was further enriched by employing Pearson correlation to discern the regulatory relationship between the differentially accumulated metabolites (DAMs) and the differentially expressed proteins (DEPs). Displayed in Fig. 6A is the correlation of the top 20 DAMs and DEPs which elucidates the regulatory associations between these DAMs and DEPs. Additionally, a Kyoto Encyclopedia of Genes and Genomes Markup Language (KGML) network was constructed based on the identified DAMs and DEPs, as represented in Fig. 6B. This aided in identifying critical nodes and metabolic pathways that were markedly overrepresented in the yielded results.

3.6. Exploration the metabolic characteristics of kidney in HN rats by fluorescence imaging and PET/CT

By integrating metabolomics and proteomics, alterations within glucose metabolism, fatty acid metabolism, and levels of oxidative phosphorylation in the kidneys of Hyperuricemic Nephropathy (HN) rats were observed. To validate the findings obtained through the omics approach, metabolic characteristics were evaluated using fluorescence imaging and PET/CT. Enhanced fluorescence intensity within the kidneys of HN rats was evident in the outcomes of fluorescence imaging using BODIPY FL C_{16} (Fig. 7A), suggesting a downregulation of fatty acid metabolism in these structures. Tetramethylrhodamine ethyl ester (TMRE), a specific fluorescent probe, was utilized to evaluate the mitochondrial membrane potential and level of oxidative phosphorylation. TMRE fluorescent imaging (Fig. 7C) revealed a significant elevation in mitochondrial membrane potential in the kidneys of HN

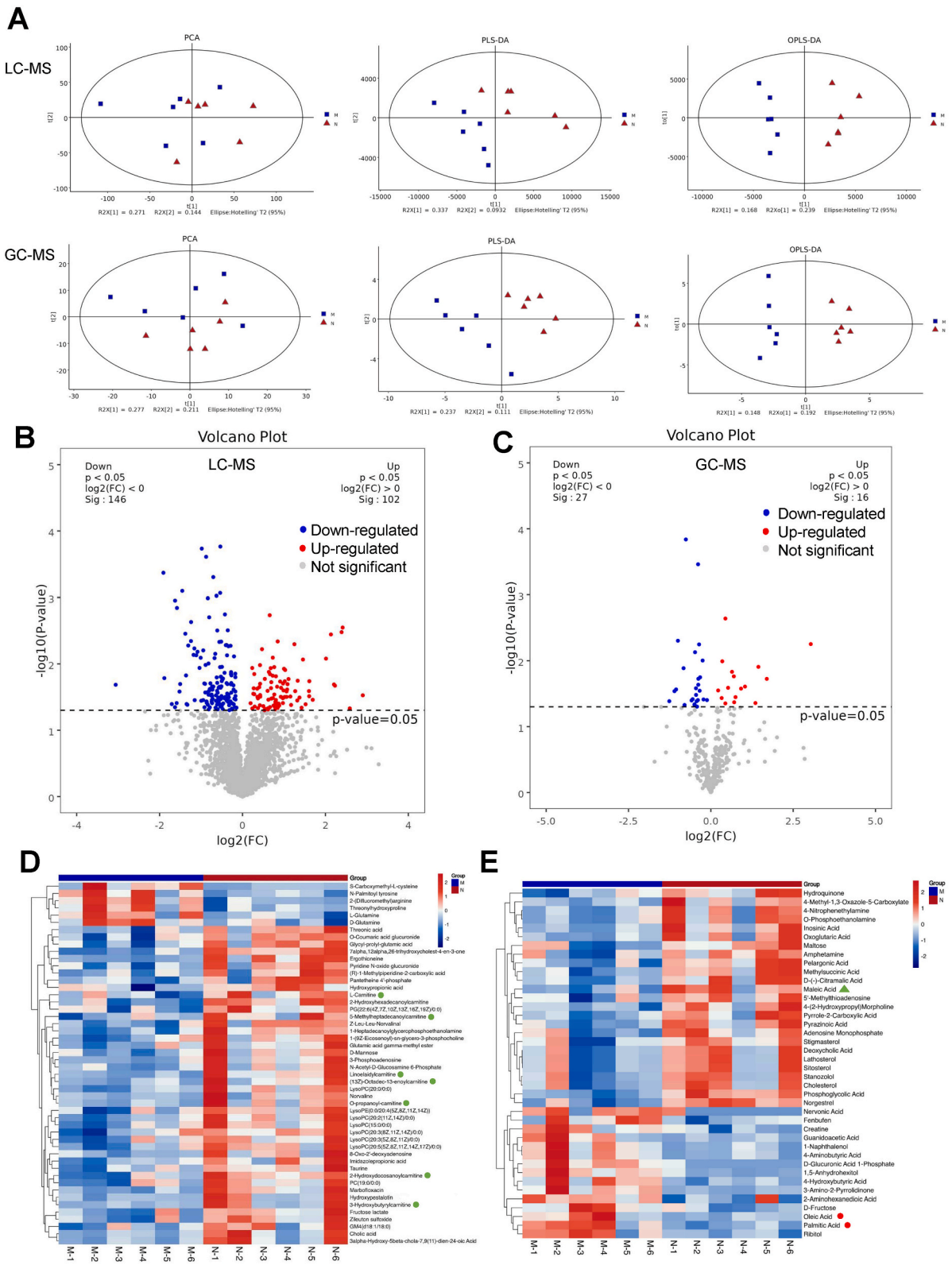

Fig. 2. Untargeted metabolomics profiling of kidney from rats with HN. (A) Principal component analysis (PCA), partial least squares discriminant analysis (PLS-DA) and orthogonal projections to latent structures-discriminant analysis (OPLS-DA) in both of LC-MS and GC-MS platforms. (B–C) The volcano plot of differentially expressed metabolites between HN and normal group in LC-MS platform (B) and GC-MS platform (C); the metabolites whose expression increased in HN are shown in red and those whose expression decreased are shown in blue. (D–E) Heatmap of differentially expressed metabolites between HN and normal group in LC-MS platform (D) and GC-MS platform (E); green dots represent decreased expression of metabolites in HN group and red dots represent increased expression of metabolites in HN group; N and M represent normal and model group, respectively. Each group of untargeted metabolomics was 6 sample replicates. (For interpretation of the references to colour in this figure legend, the reader is referred to the Web version of this article.)

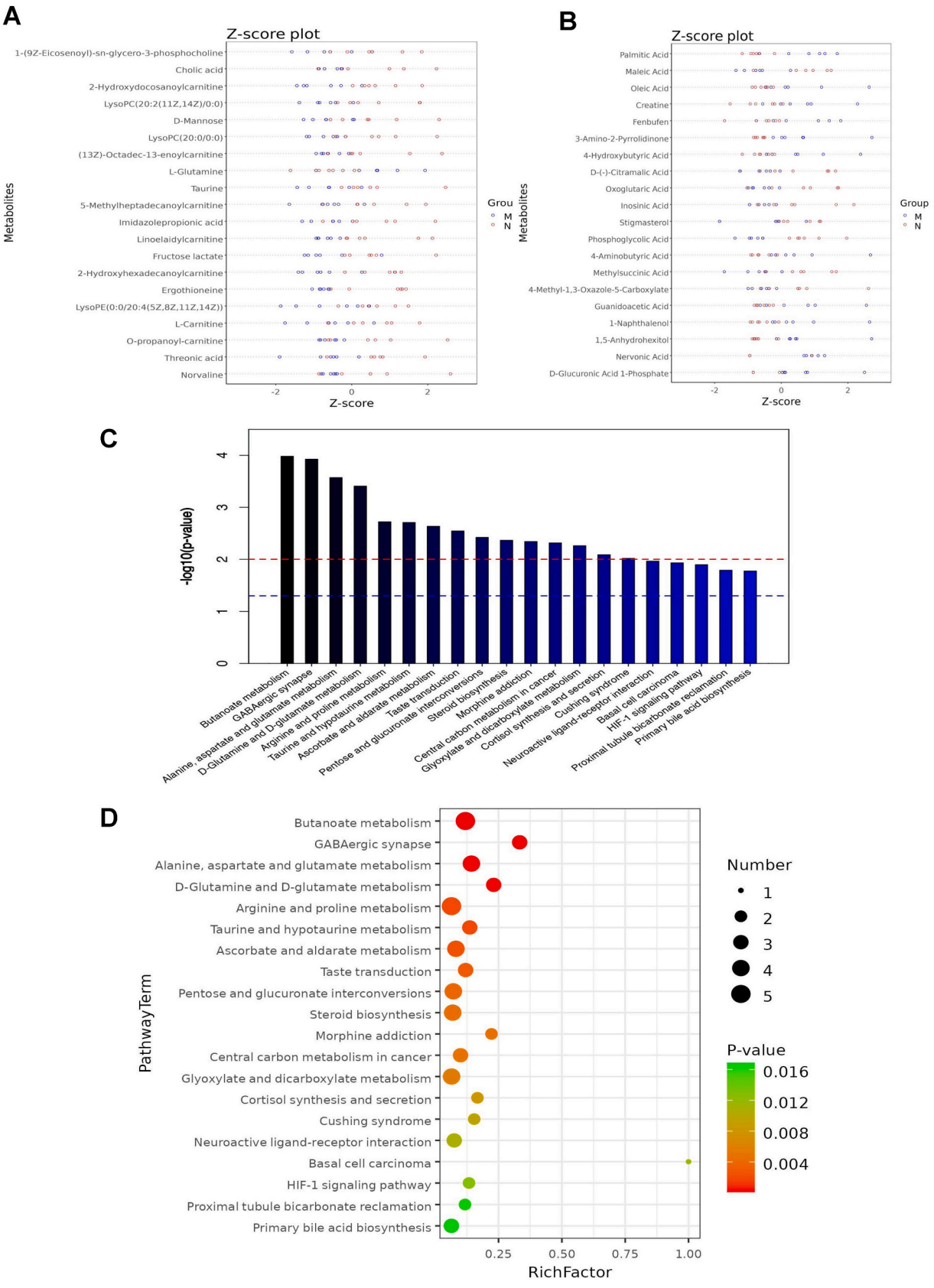

Fig. 3. Metabolic pathway enrichment analysis of untargeted metabolomics. (A–B) Z-score standardization analysis; LC-MS platform (A) and GC-MS platform (B). (C) KEGG pathway enrichment analysis; blue line represents p = 0.05 and red line represents p = 0.01. (D) Bubble chart of top 20 pathway enrichment analysis. (For interpretation of the references to colour in this figure legend, the reader is referred to the Web version of this article.)

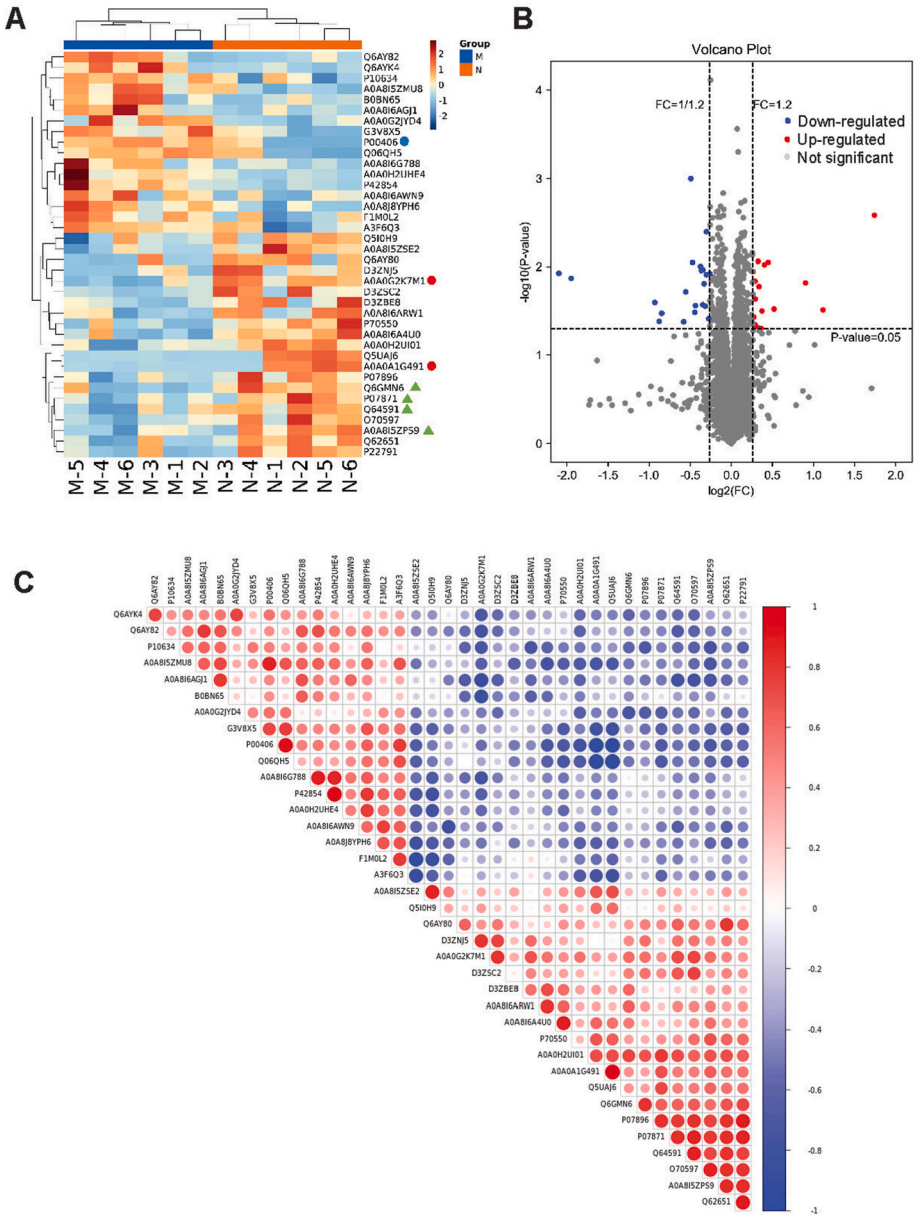

Fig. 4. Protein expression analysis. (A) Heatmap of differentially expressed proteins between HN and normal group; N and M represent normal and model group, respectively. (B) The volcano plot of differentially expressed proteins between HN and normal group; the metabolites whose expression increased in HN are shown in red and those whose expression decreased are shown in blue. (C) Correlation analysis of different expressed proteins. Each group of proteomic was 6 sample replicates. (For interpretation of the references to colour in this figure legend, the reader is referred to the Web version of this article.)

rats, correlating with an increase in oxidative phosphorylation levels. Further assessment of glucose metabolism was undertaken with ^{18}F-FDG-PET/CT (Fig. 7C), indicating a reduced capacity for glucose uptake in the kidneys of HN rats when compared to normo-uricemic counterparts. These gathered insights highlight the potential metabolic imbalance within a broader physiological context.

4. Discussion

Hyperuricemia prevalence has experienced an upward trend, which has been paralleled by an increased incidence of Hyperuricemic Nephropathy (Ejaz et al., 2020). An HPD stands as a significant contributor to the onset of hyperuricemia and HN, with long-term HPD exposure leading to consequential renal lesions and perpetuating the development of chronic kidney disease. Current research efforts predominantly examine renal function markers such as creatinine and blood urea nitrogen (BUN), while comprehensive understanding of HPD-induced kidney metabolic features remains limited. Our study therefore focuses on a HPD-induced hyperuricemic nephropathy model to delve into the impact of a HPD on renal metabolic attributes, encompassing glucose metabolism, fatty acid metabolism, and levels of oxidative phosphorylation.

Clear renal injury, as evidenced by structural damage and biochemical indicators' imbalance, was identified in HPD-induced HN rat models. Some research has pointed towards deposition of uric acid crystals in renal tissue (Grases et al., 2024), contributing to renal fibrosis and tubular necrosis (Cao et al., 2024). HPD-induced inflammatory response and oxidative stress were also identified as significant factors leading to renal damage (Wang et al., 2024). Additionally, present study indicated a disruption in urea metabolism following a two-month HPD regimen in rats, which ultimately precipitated renal damage due to elevated blood ammonia levels (Zhao et al., 2022). Despite these

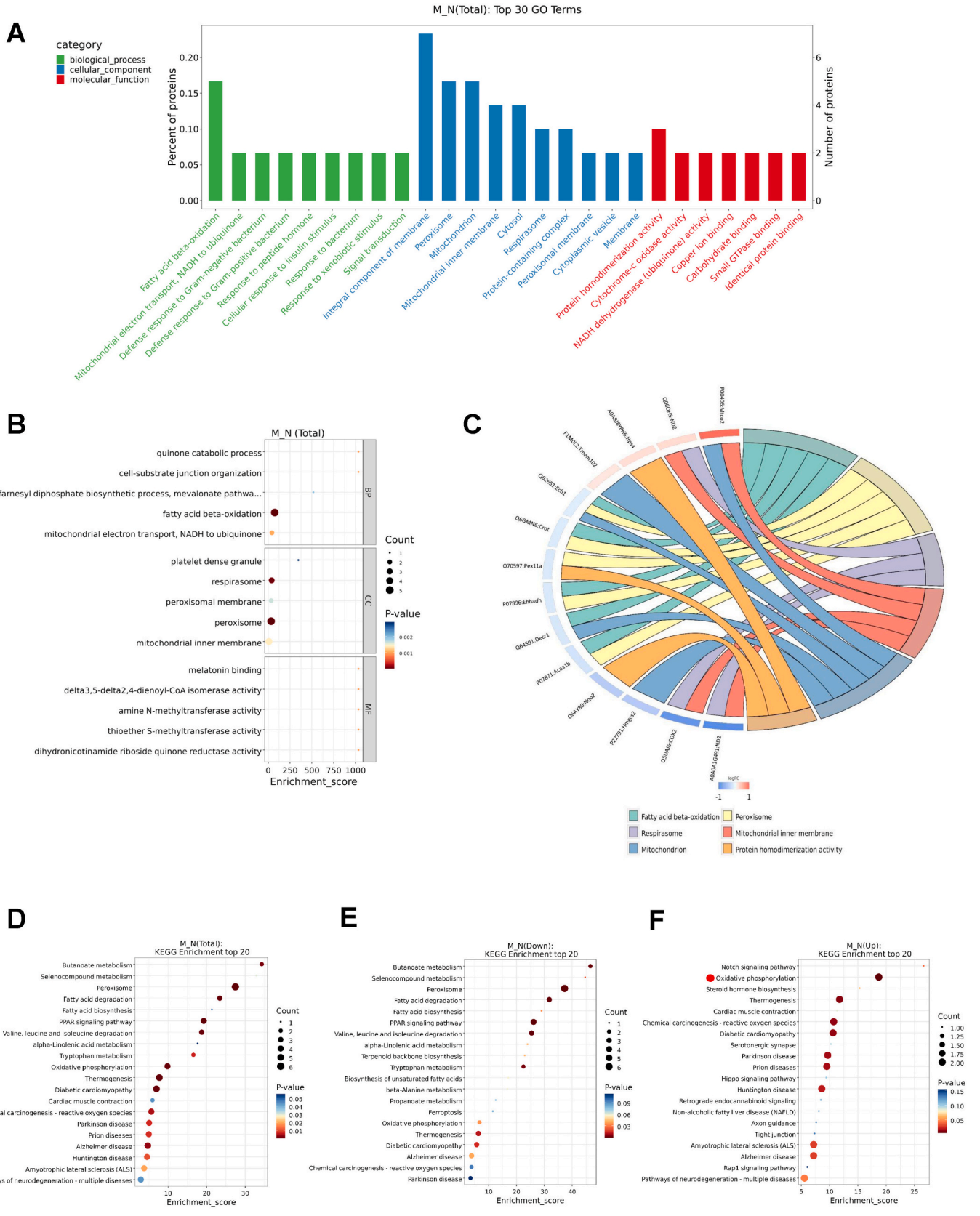

Fig. 5. Functional enrichment analysis of differentially expression proteins. (A) Gene Ontology (GO) enrichment analysis. (B) Bubble chart of top 15 GO enrichment analysis. (C) Chord Diagram of GO enrichment analysis. (D–F) Kyoto Encyclopedia of Genes and Genomes (KEGG) enrichment analysis; (D) total, pathway down-regulated in NH group (E), pathway upregulated in NH group (F); N and M represent normal and model group, respectively.

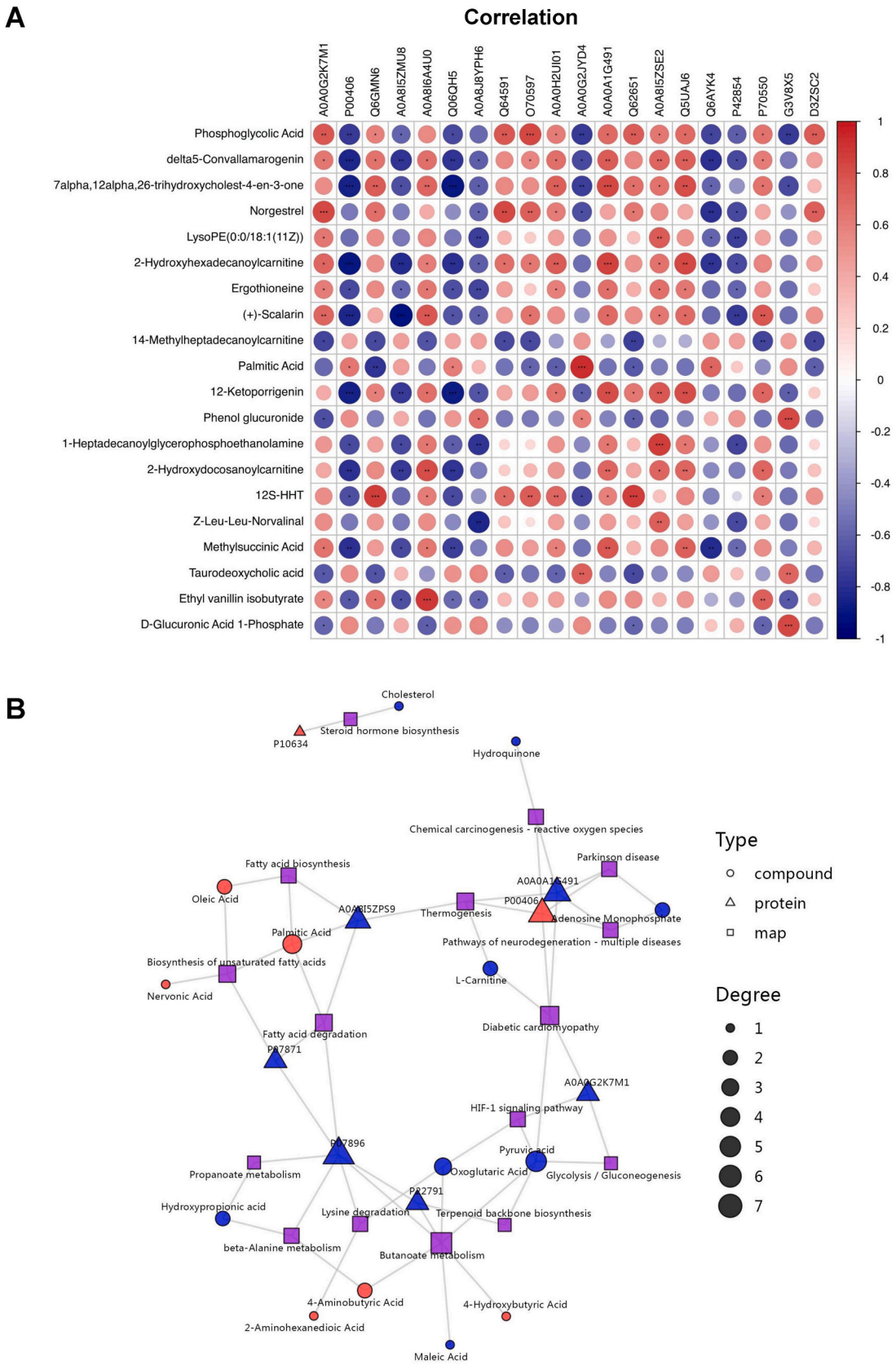

Fig. 6. Co-analysis of metabonomic and proteomic. (A) Correlation analysis of different expressed proteins and metabolites. (B) KEGG Markup Language (KGML) network analysis; the square represented the pathway, the triangle represented the protein, and the circle represented the metabolite; red indicated up-regulated proteins or metabolites and blue indicated down-regulated proteins or metabolites; degree represented the number of connections they have to each other. (For interpretation of the references to colour in this figure legend, the reader is referred to the Web version of this article.)

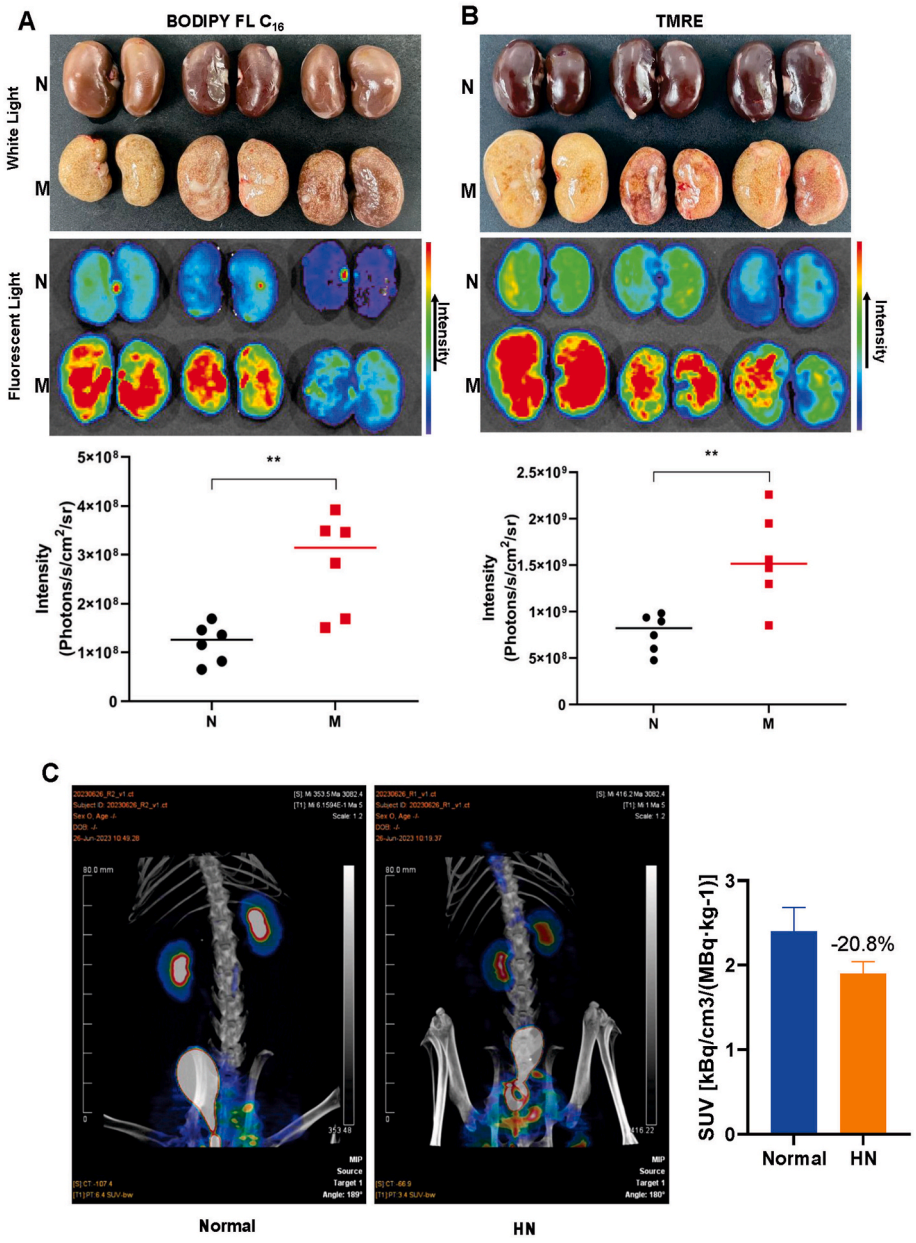

Fig. 7. Fluorescence and PET/CT imaging. (A) Fluorescence imaging of BODIPY FL C_{16}, n = 3. (B) Fluorescence imaging of TMRE, n = 3. (C) ^{18}F-FDG-PET/CT imaging, n = 1. N and M represent normal and model group, respectively.

findings, there remains a research gap regarding renal injury in hyperuricemic nephropathy.

Our investigation highlighted metabolite changes in the kidneys of HN rats through metabolomics. The identified alterations were particularly prominent in fatty acids and amino acids metabolism. Notably, we observed a marked decrease in L-carnitine, accompanied by declining levels of various fatty acylcarnitines such as o-propanoyl-carnitine, linoelaidylcarnitine, 5-methylheptadecanoylcarnitine, 2-hydroxydocosanoylcarnitine, and (13Z)-octadec-13-enoylcarnitine, among others. As the L-carnitine shuttle system is a crucial regulator of fatty acid β-oxidation, the decrease of L-carnitine and related acylcarnitines indicated a disruption in this metabolic pathway, leading to oleic acid and palmitic acid build-up in the kidney of HN rats. Accumulation of these fatty acids has previously been shown to precipitate pathologic conditions, indicating an adverse impact on lipid metabolism, insulin resistance, inflammation, fibrosis, and intracellular lipid aggregation (Iwata et al., 2024; H. Zhao et al., 2024b). Of particular note, palmitic acid accumulation has been linked to lipid droplet accumulation and stress-dependent cell senescence, while also contributing to heightened reactive oxygen species (ROS) production in podocytes and HK-2 cells (Hua et al., 2024). As a result, the proliferation of these fatty acids, as seen in our study, could instigate renal injury in HN models.

Proteomic results yielded insights into the dysregulation of energy metabolism, attributed to the imbalance of metabolic enzymes integral to fatty acid metabolism, glucose metabolism, and oxidative phosphorylation. Within fatty acid metabolism, essential metabolic enzymes, such as ACSL6, DECR1, ACAA1 and CROT, all play critical roles in fatty acid β-oxidation. Their decreased expression levels point to blockage in the fatty acid β-oxidation pathway. In terms of glucose metabolism, GAPDH serves as a vital metabolic enzyme within glycolysis, and its association with several metabolic disease pathogeneses has been established (Yan et al., 2023). The observed decline in GAPDH expression signifies an impairment in glycolytic functionality (Winterbourn et al., 2023). Intriguingly, observations regarding the alterations in

metabolic enzymes related to cellular respiration presented inconsistencies. A downregulation in the expression level of ND2, a Complex I subunit of the respiratory chain, was observed in HN rats while an upregulation in COX2 expression was also detected, complicating the understanding of the oxidative phosphorylation process' regulatory state within HN rat kidneys. COX2 is known for catalyzing electron transfers from reduced cytochrome *c* to the CuA center, subsequently flowing from the CuA site to heme a in COX1, before finally transferring to the CuB-heme a3 center, where it binds and reduces O_2 to H_2O(Nývltová et al., 2022). And ND2 plays a critical role in cellular respiration as it is a part of Complex I in the mitochondrial respiratory chain, which facilitates the transfer of electrons from NADH to ubiquinone, driving proton translocation across the inner mitochondrial membrane and contributing to the generation of ATP. Therefore, the contradiction of metabolic enzymes in the oxidative respiratory chain requires us to evaluate it at the overall level. For a holistic evaluation of these pathways related to energy metabolism, Gene Ontology (GO) and Kyoto Encyclopedia of Genes and Genomes (KEGG) enrichment analyses were conducted. Consequently, it was identified that the HPD significantly impedes the physiological processes of fatty acid β-oxidation and glycolysis. In contrast, oxidative phosphorylation demonstrated an enhancement, which could be a potential compensatory physiological alteration in response to metabolic disruptions.

To validate our findings regarding alterations in energy metabolism pathways, metabolic characteristics were examined using fluorescence imaging and ^{18}F-FDG-PET/CT at both the organ and living animal levels. We employed Bodipy FL C_{16}, an analog of fluorescent palmitic acid, to assess fatty acid intake and the β-oxidation. As revealed in Fig. 7A, pronounced fatty acid accumulation was observed in the kidneys of HN rats, suggesting HPD-induced impairment in fatty acid degradation capacity. The function of mitochondrial oxidative phosphorylation, which specifically reflects the mitochondrial membrane potential, was investigated using TMRE. Findings were congruous with Gene Ontology (GO) and Kyoto Encyclopedia of Genes and Genomes (KEGG) enrichment analysis results, with enhanced oxidative phosphorylation function evident in the kidneys of HN rats. In light of glycolysis inhibition, ^{18}F-FDG-PET/CT evaluation revealed a significant decrease in glucose metabolism capabilities. In summation, the abnormalities observed in the three energy metabolic pathways were validated through a comprehensive imaging and multi-omics analysis.

The progressive accumulation of long-chain fatty acids may detrimentally impact mitochondrial function and instigate considerable transcriptional reprogramming within lipid metabolism pathways. This disruption can lead to a subsequent reduction in fatty acid catabolism within $CD8^+$ T cells (Manzo et al., 2020). Moreover, the presence of toxic lipids and excessive lipid concentrations may negatively affect cardiac and renal functionality (D'Elia and Weinrauch, 2024). Therefore, a block in the β-oxidation emerges as a significant risk factor for the renal dysfunction observed in HN rats, and this risk is particularly relevant in the context of fatty acid accumulation. In parallel, tumor cells have been known to alternate metabolic phenotypes between glycolysis and oxidative phosphorylation to compensate for energy supply demands (Wei et al., 2024). This metabolic-switching phenomenon was also corroborated in the present study through the observed inhibition of GAPDH expression, affirming that the glycolytic process is obstructed by high-protein diets and that simultaneous enhancement in the oxidative phosphorylation process occurs. Furthermore, it should be noted that the β-oxidation of long-chain fatty acids supports over 95% of ATP production within heart and kidney mitochondria, serving as a crucial source to meet the high-energy demands of renal tubules (Panov, 2024). However, the cellular ability to degrade fatty acids diminishes significantly with cellular aging (Hammoud et al., 2024). Consequently, when β-oxidation function in kidney cells is inhibited, a potentially severe energy supply deficit may precipitate acute kidney injury in NH rats. Additionally, Peroxisome Proliferator-Activated Receptors (PPARs), significant ligand-activated transcription factors, regulate gene expression related to lipid metabolism (J. Gao and Gu, 2022). These play a crucial role in the regulation of β-oxidation. In the presented study, inhibition of the PPARs signaling pathway reduced free fatty acid β-oxidation in mitochondria, as reflected by the decrease in Cd36, Fatp-1, and Cpt1 (Chan et al., 2024). This inhibition may exacerbate the imbalance of fatty acid β-oxidation noted in HN rats. Ultimately, energy supply deficiency, accentuated by blockage in fatty acid β-oxidation, glycolysis inhibition, and compensatory enhancement of oxidative phosphorylation, emerges as a key contributing factor to kidney injury in NH rats. Clinically, hyperuricemia is usually accompanied by metabolic diseases such as diabetes, hyperlipidemia and hypertension. Therefore, renal impairment is the result of a complex combination of factors in human body. In future research, we will focus on the mechanisms of renal impairment caused by multiple chronic diseases and the contribution of the diet.

5. Conclusion

In the present investigation, a HN rat model was developed via an HPD. The study employed metabolomic and proteomic analyses to elucidate the pathological changes inherent to HN. Additionally, fluorescence imaging and ^{18}F-FDG-PET/CT were utilized to authenticate these alterations. Consequently, it was discerned that fatty acid β-oxidation and glycolysis experienced inhibitory blockages, while the function of oxidative phosphorylation showcased compensatory enhancement in HN rats. Furthermore, the inhibition of the PPARs signaling pathway aggravated the obstruction of β-oxidation function. Overall, an energy supply deficiency emerged as a crucial factor contributing to kidney injury in NH rats, thereby underscoring paying more attention to renal energy supply in the therapy of hyperuricemia nephropathy.

CRediT authorship contribution statement

Zhenxiong Zhao: Conceptualization, Methodology, Investigation, Writing – original draft, Funding acquisition. **Zhikun Li:** Methodology, Software. **Yubin Xu:** Resources, Writing – review & editing. **Shiqi Zhao:** Formal analysis, Investigation. **Qing Fan:** Conceptualization, Funding acquisition, Project administration. **Zhencang Zheng:** Supervision, Writing – review & editing.

Declaration of competing interest

The authors declare that they have no known competing financial interests or personal relationships that could have appeared to influence the work reported in this paper.

Data availability

Data for this article, including proteomics and metabolomics are available at Science Data Bank at https://www.scidb.cn/s/E7rANb.

Acknowledgment

This work was supported by National Natural Science Foundation of China (32200095and 82104051), Natural Science Foundation of Shandong Province (ZR2021QH094), Zhejiang Provincial Medical and Health Science and Technology Plan Project (2023RC111) and the Youth Innovation Science and Technology Program of Shandong Provincial Universities (2023KJ345).

Appendix A. Supplementary data

Supplementary data to this article can be found online at https://doi.org/10.1016/j.crfs.2024.100864.

References

Bardin, T., Nguyen, Q.D., Tran, K.M., Le, N.H., Do, M.D., Richette, P., Letavernier, E., Correas, J.M., Resche-Rigon, M., 2021. A cross-sectional study of 502 patients found a diffuse hyperechoic kidney medulla pattern in patients with severe gout. Kidney Int. 99 (1), 218–226.

Cao, Y., Wang, Y., Li, W., Feng, J., Chen, Y., Chen, R., Hu, L., Wei, J., 2024. Fasudil attenuates oxidative stress-induced partial epithelial-mesenchymal transition of tubular epithelial cells in hyperuricemic nephropathy via activating Nrf2. Eur. J. Pharmacol. 975, 176640.

Chan, W.S., Ng, C.F., Pang, B.P.S., Hang, M., Tse, M.C.L., Iu, E.C.Y., Ooi, X.C., Yang, X., Kim, J.K., Lee, C.W., Chan, C.B., 2024. Exercise-induced BDNF promotes PPARδ-dependent reprogramming of lipid metabolism in skeletal muscle during exercise recovery. Sci. Signal. 17 (828), eadh2783.

Chen, J., Zheng, Y., Gong, S., Zheng, Z., Hu, J., Ma, L., Li, X., Yu, H., 2023. Mechanisms of theaflavins against gout and strategies for improving the bioavailability. Phytomedicine 114, 154782.

Chen, Q., Liang, X., Wu, T., Jiang, J., Jiang, Y., Zhang, S., Ruan, Y., Zhang, H., Zhang, C., Chen, P., Lv, Y., Xin, J., Shi, D., Chen, X., Li, J., Xu, Y., 2022. Integrative analysis of metabolomics and proteomics reveals amino acid metabolism disorder in sepsis. J. Transl. Med. 20 (1), 123.

D'Elia, J.A., Weinrauch, L.A., 2024. Lipid toxicity in the cardiovascular-kidney-metabolic syndrome (CKMS). Biomedicines 12 (5).

Dalbeth, N., Gosling, A.L., Gaffo, A., Abhishek, A., 2021. Gout. Lancet 397 (10287), 1843–1855.

Ejaz, A.A., Nakagawa, T., Kanbay, M., Kuwabara, M., Kumar, A., Garcia Arroyo, F.E., Roncal-Jimenez, C., Sasai, F., Kang, D.H., Jensen, T., Hernando, A.A., Rodriguez-Iturbe, B., Garcia, G., Tolan, D.R., Sanchez-Lozada, L.G., Lanaspa, M.A., Johnson, R. J., 2020. Hyperuricemia in kidney disease: a major risk factor for cardiovascular events, vascular calcification, and renal damage. Semin. Nephrol. 40 (6), 574–585.

Gao, J., Gu, Z., 2022. The role of peroxisome proliferator-activated receptors in kidney diseases. Front. Pharmacol. 13, 832732.

Gao, Y.F., Liu, M.Q., Li, Z.H., Zhang, H.L., Hao, J.Q., Liu, B.H., Li, X.Y., Yin, Y.Q., Wang, X.H., Zhou, Q., Xu, D., Shi, B.M., Zhang, Y.H., 2023. Purification and identification of xanthine oxidase inhibitory peptides from enzymatic hydrolysate of α-lactalbumin and bovine colostrum casein. Food Res. Int. 169, 112882.

Grases, F., Tomàs Nadal, F., Julià Florit, F., Costa-Bauza, A., 2024. Cystine renal calculi: new aspects related to their formation and development. J. Clin. Med. 13 (10), 2837.

Hammoud, S., Ivanova, A., Osaki, Y., Funk, S., Yang, H., Viquez, O., Delgado, R., Lu, D., Phillips Mignemi, M., Tonello, J., Colon, S., Lantier, L., Wasserman, D.H., Humphreys, B.D., Koenitzer, J., Kern, J., de Caestecker, M., Finkel, T., Fogo, A., Messias, N., Lodhi, I.J., Gewin, L.S., 2024. Tubular CPT1A deletion minimally affects aging and chronic kidney injury. JCI Insight 9 (6), e171961.

Hao, L., Ding, Y., Fan, Y., Tian, Q., Liu, Y., Guo, Y., Zhang, J., Hou, H., 2024. Identification of hyperuricemia alleviating peptides from yellow tuna Thunnus albacares. J. Agric. Food Chem. 72 (21), 12083–12099.

He, B., Nie, Q., Wang, F., Wang, X., Zhou, Y., Wang, C., Guo, J., Fan, X., Ye, Z., Liu, P., Wen, J., 2023. Hyperuricemia promotes the progression of atherosclerosis by activating endothelial cell pyroptosis via the ROS/NLRP3 pathway. J. Cell. Physiol. 238 (8), 1808–1822.

Hou, Z., Ma, A., Mao, J., Song, D., Zhao, X., 2023. Overview of the pharmacokinetics and pharmacodynamics of URAT1 inhibitors for the treatment of hyperuricemia and gout. Expet Opin. Drug Metabol. Toxicol. 19 (12), 895–909.

Hua, W., Peng, L., Chen, X.M., Jiang, X., Hu, J., Jiang, X.H., Xiang, X., Wan, J., Long, Y., Xiong, J., Ma, X., Du, X., 2024. CD36-mediated podocyte lipotoxicity promotes foot process effacement. Open Med. 19 (1), 20240918.

Iwata, A., Maruyama, J., Natsuki, S., Nishiyama, A., Tamura, T., Tanaka, M., Shichino, S., Seki, T., Komai, T., Okamura, T., Fujio, K., Tanaka, M., Asano, K., 2024. Egr2 drives the differentiation of Ly6C(hi) monocytes into fibrosis-promoting macrophages in metabolic dysfunction-associated steatohepatitis in mice. Commun. Biol. 7 (1), 681.

Joosten, L.A.B., Crişan, T.O., Bjornstad, P., Johnson, R.J., 2020. Asymptomatic hyperuricaemia: a silent activator of the innate immune system. Nat. Rev. Rheumatol. 16 (2), 75–86.

Kim, S.M., Lee, S.H., Kim, Y.G., Kim, S.Y., Seo, J.W., Choi, Y.W., Kim, D.J., Jeong, K.H., Lee, T.W., Ihm, C.G., Won, K.Y., Moon, J.Y., 2015. Hyperuricemia-induced NLRP3 activation of macrophages contributes to the progression of diabetic nephropathy. Am. J. Physiol. Ren. Physiol. 308 (9), F993–f1003.

Li, L., Zhao, K., Luo, J., Tian, J., Zheng, F., Lin, X., Xie, Z., Jiang, H., Li, Y., Zhao, Z., Wu, T., Pang, J., 2024. Piperine improves hyperuricemic nephropathy by inhibiting URAT1/GLUT9 and the AKT-mTOR pathway. J. Agric. Food Chem. 72 (12), 6565–6574.

Liu, B., Zhao, L., Yang, Q., Zha, D., Si, X., 2021. Hyperuricemia and hypertriglyceridemia indicate tubular atrophy/interstitial fibrosis in patients with IgA nephropathy and membranous nephropathy. Int. Urol. Nephrol. 53 (11), 2321–2332.

Lubawy, M., Formanowicz, D., 2023. High-fructose diet-induced hyperuricemia accompanying metabolic syndrome-mechanisms and dietary therapy proposals. Int. J. Environ. Res. Publ. Health 20 (4), 3596.

Manzo, T., Prentice, B.M., Anderson, K.G., Raman, A., Schalck, A., Codreanu, G.S., Nava Lauson, C.B., Tiberti, S., Raimondi, A., Jones, M.A., Reyzer, M., Bates, B.M., Spraggins, J.M., Patterson, N.H., McLean, J.A., Rai, K., Tacchetti, C., Tucci, S., Wargo, J.A., Rodighiero, S., Clise-Dwyer, K., Sherrod, S.D., Kim, M., Navin, N.E., Caprioli, R.M., Greenberg, P.D., Draetta, G., Nezi, L., 2020. Accumulation of long-chain fatty acids in the tumor microenvironment drives dysfunction in intrapancreatic CD8+ T cells. J. Exp. Med. 217 (8), e20191920.

McCormick, N., Choi, H.K., 2024. Recurrent gout and serum urate-reply. JAMA 331 (20), 1768–1769.

Mehmood, A., Iftikhar, A., Chen, X., 2024. Food-derived bioactive peptides with anti-hyperuricemic activity: a comprehensive review. Food Chem. 451, 139444.

Nývltová, E., Dietz, J.V., Seravalli, J., Khalimonchuk, O., Barrientos, A., 2022. Coordination of metal center biogenesis in human cytochrome c oxidase. Nat. Commun. 13 (1), 3615.

Pan, L., Han, P., Ma, S., Peng, R., Wang, C., Kong, W., Cong, L., Fu, J., Zhang, Z., Yu, H., Wang, Y., Jiang, J., 2020. Abnormal metabolism of gut microbiota reveals the possible molecular mechanism of nephropathy induced by hyperuricemia. Acta Pharm. Sin. B 10 (2), 249–261.

Panov, A.V., 2024. The structure of the cardiac mitochondria respirasome is adapted for the β-oxidation of fatty acids. Int. J. Mol. Sci. 25 (4), 2410.

Qi, X., Li, Q., Che, X., Wang, Q., Wu, G., 2021. The uniqueness of clear cell renal cell carcinoma: summary of the process and abnormality of glucose metabolism and lipid metabolism in ccRCC. Front. Oncol. 11, 727778.

Qiao, P., Sun, Y., Wang, Y., Lin, S., An, Y., Wang, L., Liu, J., Huang, Y., Yang, B., Zhou, H., 2023. Activation of NRF2 signaling pathway delays the progression of hyperuricemic nephropathy by reducing oxidative stress. Antioxidants 12 (5), 1022.

Tran, D.H., Kim, D., Kesavan, R., Brown, H., Dey, T., Soflaee, M.H., Vu, H.S., Tasdogan, A., Guo, J., Bezwada, D., Al Saad, H., Cai, F., Solmonson, A., Rion, H., Chabatya, R., Merchant, S., Manales, N.J., Tcheuyap, V.T., Mulkey, M., Mathews, T. P., Brugarolas, J., Morrison, S.J., Zhu, H., DeBerardinis, R.J., Hoxhaj, G., 2024. De novo and salvage purine synthesis pathways across tissues and tumors. Cell 187 (14), 3602–3618.e20.

Wang, Z., Huang, Y., Yang, T., Song, L., Xiao, Y., Chen, Y., Chen, M., Li, M., Ren, Z., 2024. Lactococcus cremoris D2022 alleviates hyperuricemia and suppresses renal inflammation via potential gut-kidney axis. Food Funct. 15 (11), 6015–6027.

Wei, X., Han, R., Gao, Y., Song, P., Guo, Z., Hou, Y., Yu, J., Tang, K., 2024. Boosting energy deprivation by synchronous interventions of glycolysis and oxidative phosphorylation for bioenergetic therapy synergetic with chemodynamic/photothermal therapy. Adv. Sci. 11 (23), e2401738.

Winterbourn, C.C., Peskin, A.V., Kleffmann, T., Radi, R., Pace, P.E., 2023. Carbon dioxide/bicarbonate is required for sensitive inactivation of mammalian glyceraldehyde-3-phosphate dehydrogenase by hydrogen peroxide. Proc. Natl. Acad. Sci. U.S.A. 120 (18), e2221047120.

Xiong, C., Deng, J., Wang, X., Hou, Q., Zhuang, S., 2024. Pharmacological inhibition of Src family kinases attenuates hyperuricemic nephropathy. Front. Pharmacol. 15, 1352730.

Yan, Z., Cao, X., Sun, S., Sun, B., Gao, J., 2023. Inhibition of GSK3B phosphorylation improves glucose and lipid metabolism disorder. Biochim. Biophys. Acta, Mol. Basis Dis. 1869 (6), 166726.

Yang, Y., Lin, Q., Zhu, X., Shao, X., Li, S., Li, J., Wu, J., Jin, H., Qi, C., Jiang, N., Zhang, K., Wang, Q., Gu, L., Ni, Z., 2024. Activation of lipophagy is required for RAB7 to regulate ferroptosis in sepsis-induced acute kidney injury. Free Radic. Biol. Med. 218, 120–131.

Zhao, H., Zhai, B.W., Zhang, M.Y., Huang, H., Zhu, H.L., Yang, H., Ni, H.Y., Fu, Y.J., 2024a. Phlorizin from Lithocarpus litseifolius [Hance] Chun ameliorates FFA-induced insulin resistance by regulating AMPK/PI3K/AKT signaling pathway. Phytomedicine 130, 155743.

Zhao, X., Li, Y., Yu, J., Teng, H., Wu, S., Wang, Y., Zhou, H., Li, F., 2024b. Role of mitochondria in pathogenesis and therapy of renal fibrosis. Metabolism, 155913.

Zhao, Z.X., Tang, X.H., Jiang, S.L., Pang, J.Q., Xu, Y.B., Yuan, D.D., Zhang, L.L., Liu, H. M., Fan, Q., 2022. Astragaloside IV improves the pharmacokinetics of febuxostat in rats with hyperuricemic nephropathy by regulating urea metabolism in gut microbiota. Front. Pharmacol. 13, 1031509.